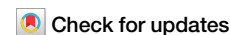


<https://doi.org/10.1038/s41524-024-01504-2>

# Excitons in nonlinear optical responses: shift current in MoS<sub>2</sub> and GeS monolayers



J. J. Esteve-Paredes<sup>1</sup>✉, M. A. García-Blázquez<sup>1</sup>, A. J. Uriá-Álvarez<sup>1</sup>, M. Camarasa-Gómez<sup>1,2</sup> & J. J. Palacios<sup>1,3,4</sup>

It is well-known that exciton effects are determinant to understanding the optical absorption spectrum of low-dimensional materials. However, the role of excitons in nonlinear optical responses has been much less investigated at the experimental level. Additionally, computational methods to calculate nonlinear conductivities in real materials are still not widespread, particularly taking into account excitonic interactions. We present a methodology to calculate the excitonic second-order optical responses in 2D materials relying on: (i) *ab initio* tight-binding Hamiltonians obtained by Wannier interpolation and (ii) solving the Bethe-Salpeter equation with effective electron-hole interactions. Here, in particular, we explore the role of excitons in the shift current of monolayer materials. Focusing on MoS<sub>2</sub> and GeS monolayer systems, our results show that *2p*-like excitons, which are dark in the linear response regime, yield a contribution to the photocurrent comparable to that of *1s*-like excitons. Under radiation with intensity  $\sim 10^4 \text{ W/cm}^2$ , the excitonic theory predicts in-gap photogalvanic currents of almost  $\sim 10 \text{ nA}$  in sufficiently clean samples, which is typically one order of magnitude higher than the value predicted by independent-particle theory near the band edge.

Excitons are key to our understanding of the linear optical response in low-dimensional semiconductors and insulators. Examples can be found in nanotubes<sup>1,2</sup> and quasi-two-dimensional (2D) crystals<sup>3,4</sup>. In these systems, the combined effect of quantum confinement and a weak screening environment lead to large excitonic binding energies<sup>5–7</sup>. This fact manifests in strong peaks below the quasi-particle gap in photoluminescence and optical absorption experiments. From the theory point of view, the linear response formalism plus the Bethe-Salpeter equation (BSE) for exciton calculations have been proven to be powerful tools to explain the measured optical responses in the low-field regime<sup>8–14</sup>.

In the nonlinear regime, the bulk photovoltaic or photogalvanic effect<sup>15</sup> (abbreviated BPVE or PGE) is a nonlinear effect of the second order that has attracted much interest lately (see ref. 16 for a review). It refers to the generation of a direct current (DC) in the bulk of a non-centrosymmetric material under light radiance, and thus it has an inherent potential for application in solar-cell devices. The BPVE was early explored in ferroelectric materials<sup>17,18</sup>, and continued gathering attention during the next decades<sup>19–23</sup> until nowadays, as experiments achieve a high-efficiency in power conversion<sup>24</sup>. More recently, low-dimensional materials have also been explored in this regard. For instance, it has been shown that a large BPVE occurs in WS<sub>2</sub> nanotubes<sup>25,26</sup> and nanoribbons<sup>27</sup>, strained 3R-MoS<sub>2</sub>

and phosphorene<sup>28,29</sup>, monolayer MoSe<sub>2</sub><sup>30</sup>, SnS<sup>31,32</sup>, or one-dimensional grain boundaries<sup>33</sup>.

The characterization and rationalization of the experimental signatures of the BPVE is a current active field of research. On the theoretical side, early studies considered different mechanisms responsible for the total BPVE, including: (i) the shift current (defined below), as originating from the electronic excitation processes, (ii) the recombination current, and (iii) the ballistic current<sup>15</sup>, stemming from the asymmetry of momentum distributions of charge carriers. Results were provided showing that the ballistic current can exceed the shift current in some scenarios<sup>15</sup>. On the other hand, last-decade studies have focused on studying the shift current response through *ab initio* methods within the independent-particle approximation (IPA) for the band structure and Bloch eigenstates<sup>34–44</sup>. Even though this methodology ignores the ballistic and recombination contributions to the BPVE, it is sometimes quite successful in explaining experimental results, specially in bulk materials<sup>35,45–47</sup>. On the other hand, in other experiments the measured values of the photogalvanic currents are nearly one order of magnitude different than the predicted ones<sup>25,26</sup>, or show features that may indicate the need to go beyond a mean-field description of the problem, for instance, by including exciton effects<sup>48</sup>. As already pointed out<sup>49</sup>, there is thus a need to develop a complete theoretical framework, that allows to study real

<sup>1</sup>Departamento de Física de la Materia Condensada, Universidad Autónoma de Madrid, Madrid, Spain. <sup>2</sup>Department of Molecular Chemistry and Materials Science, Weizmann Institute of Science, Rehovot, Israel. <sup>3</sup>Instituto Nicolás Cabrera (INC), Universidad Autónoma de Madrid, Madrid, Spain. <sup>4</sup>Condensed Matter Physics Center (IFIMAC), Universidad Autónoma de Madrid, Madrid, Spain. ✉e-mail: [juan.esteve@uam.es](mailto:juan.esteve@uam.es)

materials from an ab initio perspective and capture all relevant physical ingredients in the BPVE.

Here, we focus on the inclusion of electron-hole interactions in the shift current response, which corresponds to the coherent contribution to the second-order DC response in the absence of magnetism and under radiation with linearly polarized light. In the literature, a few works have started considering the effect of excitons within the coherent nonlinear optical response formalism and its application to the BPVE.<sup>50–52</sup> Additionally, the role of excitons in the photogalvanic effect has been investigated by ab initio Green's function methods in the time domain<sup>53,54</sup>. Similar techniques are used for the exploration of exciton effects in the second-harmonic generation<sup>55–58</sup>. These few works show that excitons are equally or even more dominant in the nonlinear response of low-dimensional materials than in the linear response.

In this work, we present a methodology to compute the second-order optical conductivity which takes into account electron-hole interactions, updating previous approaches to linear optical properties based on tight-binding methods<sup>9–11,59–61</sup>. Here we start from an ab initio tight-binding description of the band structure, obtained by Wannier interpolation. Importantly, the use of a Wannier Hamiltonian ensures that all relevant dipole matrix elements in the local basis are properly accounted for, which gives a description of optical responses more accurately than a purely effective tight-binding approximation<sup>62–64</sup>. Secondly, electron-hole interactions are included by solving the BSE with effectively-screened electron-hole interactions. As a proof of concept, we focus on the evaluation of the (DC) shift current response. This current response is clearly discernible in experiments and understood with theoretical calculations<sup>17,18,35,45,47,48</sup>.

As case examples, we study MoS<sub>2</sub> and GeS monolayers. The former is a prototypical TMDC material, showing a rich structure of exciton levels due to the important role played by spin-orbit coupling (SOC), while the latter is often taken as a test case for its simplicity and possibly very large shift current<sup>36,37,53,53,63</sup>. We compute the shift current as a function of the frequency of the incident radiation, as it would be measured in a photocurrent spectroscopy experiment<sup>25,30</sup>. We show that excitonic effects red-shift the IPA frequency-dependent response function, generally increasing the shift current by nearly an order of magnitude. This happens by the appearance of a finite and sometimes dominant contribution at energies below the band gap. Interestingly, we also show that *2p*-like excitons, dark in linear response, are *bright* in the second-order optical response and, therefore, can contribute to the BPVE.

## Results and discussion

### Band structure and excitons

We start by calculating the quasi-particle band structure of the two case examples monolayer materials. We consider the *2H* phase of MoS<sub>2</sub>, with *D*<sub>3h</sub> point group, and monolayer GeS, with *C*<sub>2v</sub> point group (as exfoliated from the  $\alpha$ -*Pnma* bulk phase<sup>36,65</sup>). In Fig. 1a we show the band structure for the former, calculated using a SRSF functional<sup>66,67</sup>. This functional yields a direct gap of 2.60 eV at the *K* point. More details about this methodology are given in Sec. Methods. We include SOC in the calculation, yielding a top valence band splitting of 0.17 eV. These values are in good agreement with previous calculations (see e.g., refs. 12,13). In Fig. 1b, we show the band structure of GeS, as calculated using the SRSF functional, with no SOC in this case as it is expected to be small. Our calculations yield a direct gap at  $\Gamma$  of 2.72 eV, in good agreement with previous calculations<sup>68</sup>.

In a post-processing step, we obtain a Wannier-interpolated Hamiltonian<sup>69,70</sup> for both materials. Next, we include exciton effects by solving the BSE. To perform this task, we evaluate the electron-hole interaction matrix elements by employing a Rytova-Keldysh potential, which is suitable for monolayer materials. We make use of the tight-binding-like character of Wannier functions to evaluate Coulomb matrix elements using a real-space implementation<sup>61</sup>. More details are given in Sec. Methods.

We now review the main features of the excitons in MoS<sub>2</sub>, based on the output of our methodology. For further analysis, we name the energy bands as ( $v_{-1}$ ,  $v_0$ ,  $c_1$ ,  $c_2$ ) in order of increasing energy at the *K* point. To understand

the exciton spectrum, special attention needs to be paid to the spin structure of the BSE. Since  $S_z$  is a good quantum number in the vicinity of the *K* and *K'* points, the interacting BSE Hamiltonian almost decouples into a set of solutions with like or unlike-spin of electron-hole pairs. Only excitons formed by spin-conserving electron-hole pairs are expected to have enough oscillator strength to be bright through light-matter interaction. The SOC-induced band split gives rise to two series of excitons. Around the *K* point, the lowest-energy electron-hole pair excitation with the same spin is ( $v_0$ ,  $c_1$ ). Accordingly, equal-energy electron-hole excitations occur at *K'* with inverted spin character, due to time reversal symmetry. Excitons that are mainly formed by these electron-hole free pairs constitute the A series. The next like-spin free electron-hole excitations, ( $v_{-1}$ ,  $c_2$ ) gives a different series of excitons, called B. Within the A series, we find the following structure for the exciton shell structure: 1s at 2.00 eV, 2p at 2.26 eV, 2s at 2.32 eV, 3d at 2.37 eV, and 3s at 2.43 eV. A similar series, called B, is found blueshifted by an amount of ~0.17 eV, which corresponds to the SOC split of the 1s exciton. The angular momenta character is assigned by inspecting the node structure of  $A_{vc}^{(N)}(\mathbf{k})$ . Our numerical results show that the lowest-energy exciton of the spectrum is formed by unlike-spin transitions around *K* and *K'* valleys, redshifted from the optically bright A-1s exciton by 25 meV. The previous spin structure of levels and our numerical results are in very good agreement with ab initio, tight-binding and model calculations<sup>7,10–12,59,71</sup>.

In the case of GeS and according to Fig. 1b, the lowest-energy and direct electron-hole excitation across the band-gap occur at  $\Gamma$ , followed by an excitation along the  $\Gamma$ -X path, which we denote with  $V_x$  (using the same notation as in<sup>72</sup>). As a consequence, our calculations show that the first five bound exciton states are formed by a linear combination of *e-h* pairs around  $\Gamma$ , while the fifth in energy is formed in the  $V_x$  region. We label them according to its angular momentum character:  $\Gamma$ -1s at 1.82 eV,  $\Gamma$ -2p<sub>1</sub> at 2.11 eV,  $\Gamma$ -2p<sub>2</sub> at 2.21 eV,  $\Gamma$ -3p at 2.26 eV, and  $V_x$ -1s at 2.36 eV. The order of exciton levels and their angular momentum character are in complete agreement with purely ab initio calculations in ref. 68.

### Linear absorbance

We now examine the frequency-dependent absorbance of monolayer MoS<sub>2</sub>, which is based on the evaluation of the linear conductivity, as detailed in Supplementary Note 1. For the current analysis, we calculate the frequency-dependent spectrum both in the IPA approximation and after including excitons. We set a broadening  $\eta = 25$  meV throughout the rest of the work.

In Fig. 2a, we show the frequency-dependent absorbance of light under linearly polarized light. The IPA curve displays a typical step-like shape up to our range of inspection, as more bands come into play in the  $M - K - \Gamma$  path. When interactions are considered, the bright excitons become visible below the quasi-particle band gap. In single-layer MoS<sub>2</sub>, with *D*<sub>3h</sub> point group, selection rules indicate that in the bound exciton part of the spectrum, both *s* and *p* excitons are indeed optically-active<sup>73–75</sup>. However, due to the small trigonal warping effect in MoS<sub>2</sub> around the *K* point, the *p*-type excitons have a very low oscillator strength and are in practice *dark* in light absorption experiments, while only *s*-type excitons are *bright*, in agreement with our numerical calculations. As discussed, SOC induces two series of excitons which are clearly identified. Higher in energy, we identify the noticeable C resonance around 3 eV, which corresponds to the excitons formed by electron-hole pairs in the continuum. Previous studies have shown that more bands are needed in order to fully resolve the magnitude of the C resonance<sup>10</sup>, hence we do not analyze it here any further.

Figure 2b shows the optical absorbance with and without exciton effects, using light polarized along the armchair (aligned with the *x* axis) and zigzag directions of monolayer GeS. The case of armchair polarization shows two big peaks that are assigned to the  $\Gamma$ -1s and  $V_x$ -1s excitons. Remarkably, the  $\Gamma$ -3p exciton is also considerably bright, which denotes the departure from the isotropic and hydrogen-like model for excitons. The zigzag case, shown in Fig. 2c, exhibits an almost dark in-gap spectrum. We identify the first peak with the  $\Gamma$ -2p<sub>1</sub>, whose oscillator strength is appreciable in this case. The  $\Gamma$ -2p<sub>2</sub> presents the lowest oscillator strength, and it is not appreciable in absorbance either with armchair or zigzag light polarizations.

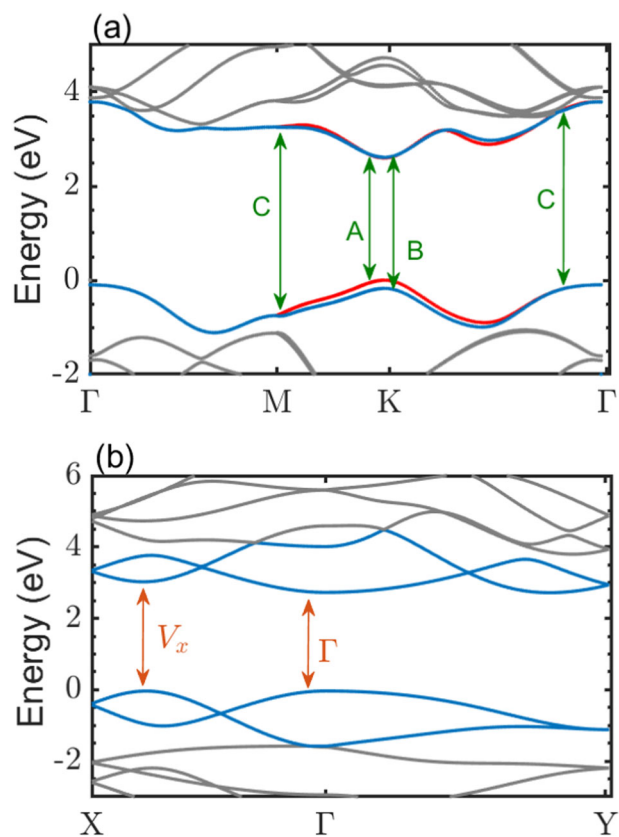


**Fig. 1 | Band structures of monolayer MoS<sub>2</sub> and monolayer GeS.** **a** Band structure of monolayer MoS<sub>2</sub> including SOC. Blue (red) bands have their eigenstates formed by mostly spin-up (spin-down) Bloch-Wannier states. We have pointed the position of the most relevant electron-hole excitation to the wavefunction of the labeled excitons in the absorbance spectrum (see Fig. 2). Bands that are not included in the BSE calculation are in gray color. **b** Same as (a) for monolayer GeS. SOC has not been included in this case.

### Shift conductivity

We now turn into the main set of results of this work, in regards to the nonlinear optical response. We develop a post-processing tool to evaluate the second-order optical conductivity with and without exciton effects, from which the shift conductivity can be extracted, as explained in Sec. Methods. Exciton effects on this quantity have been only explored in a few cases<sup>50–52</sup>. Additionally, the shift current response of monolayer GeS in presence of exciton effects has been investigated using an ab initio time-dependent scheme<sup>53</sup>. Our analysis below, based on the second order conductivity, adds extra insightful information about the relevant excitons that give rise to large shift conductivity peaks.

In the case of MoS<sub>2</sub>, if the  $x$  axis is along the armchair direction, by invoking the  $D_{3h}$  point group one can show that the only finite conductivity tensor components are  $\sigma_{xxx} = -\sigma_{xyy} = -\sigma_{yx} = -\sigma_{xy}$ . We therefore restrict our analysis to  $\sigma_{xxx}$ . Analogously, in GeS the non-vanishing purely-in-plane components of the shift conductivity are  $\sigma_{xxx}, \sigma_{xyy}, \sigma_{yx} = \sigma_{xy}$ , where the  $c_2$  rotation axis of the  $C_{2v}$  point group is taken along the  $x$  (in-plane) direction<sup>76</sup>. Note that the symmetry arguments to determine the shape of the tensor are the same as in the single-particle picture, since they can be made from Eq. (8). Below, we present results neglecting the exchange interaction in the BSE, which is a common assumption in the literature when using effective models. Actually, the inclusion of the exchange interaction noticeably changes the results, as we show in Supplementary Note 2, although our discussion here is equally valid with and without exchange effects. A more in-depth examination on the role of the exchange interaction is postponed for future work.

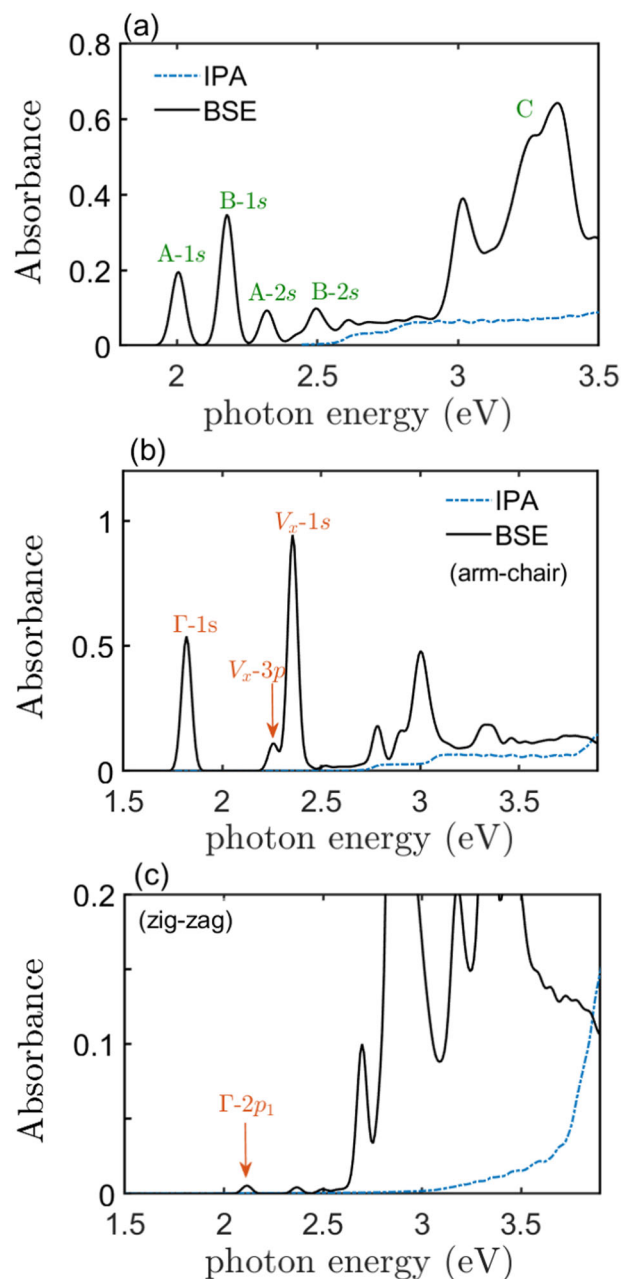


**Fig. 2 | Linear absorbance of monolayer MoS<sub>2</sub> and monolayer GeS.** **a** Linear absorbance of monolayer MoS<sub>2</sub> as calculated in the independent-particle approximation and including exciton effects. **b** Same than (a) for monolayer GeS for light polarized in the armchair direction. **c** Same as (b) but for zigzag polarization.

In Fig. 3, we show  $\sigma_{xxx}^{(sh)}(0; \omega, -\omega)$  for monolayer MoS<sub>2</sub>, as computed in the IPA, using Eq. (9), and including exciton effects, using Eq. (11). The IPA shift conductivity is positive and barely varying in the shown energy range. Interactions red-shift features that can be found in the IPA calculations at larger energies (see the SM, Sec. IV, for an extended IPA curve), bringing them into the selected energy window, while adding new ones. First, we identify the in-gap exciton resonances and label its angular momentum character. We observe that the A-1s and B-1s resonances have a response of  $\sim 8 \text{ nm} \cdot \mu\text{A}/\text{V}^2$ , which is roughly 3 times bigger than the IPA response near the band-gap. Differently from the linear absorbance case, we observe peaks corresponding to  $p$  excitons. This feature can be understood by comparing the expressions of the linear and nonlinear oscillator strengths, and the magnitude of dipole matrix elements between exciton states. In MoS<sub>2</sub>, the low trigonal warping around the  $K$  points yields that

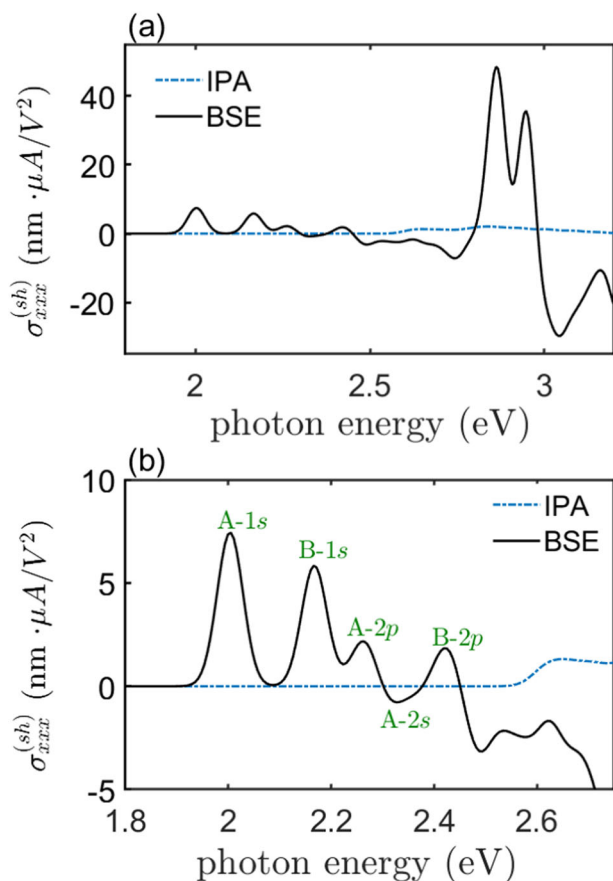


**Fig. 3 | Shift conductivity of monolayer MoS<sub>2</sub>.** **a** Frequency-dependent shift conductivity of monolayer MoS<sub>2</sub> calculated in the IPA approximation and including exciton effects. See main text for discussion. **b** In-gap excitonic shift conductivity, as zoomed in from (a). Resonances are labeled according to the exciton spectrum.

$|R_{0,2p}| \approx 0.05|R_{0,1s}|$ , and as the linear oscillator strength is  $\sim |R_{0N}|^2$ , the brightness of  $p$  excitons is strongly suppressed with respect to  $s$  excitons. In contrast, the nonlinear oscillator strength behaves as  $S_{NN'} \sim R_{0N}R_{NN'}R_{N'0}$  (normalized to the total volume). The similar value of the conductivity for the  $1s$  and  $2p$  excitons is understood by inspecting their coupling matrix elements. Our results yield that  $|R_{1s,1s}|$  and  $|R_{2s,2p}|$  are particularly small, so inter-exciton couplings are responsible for the finite shift conductivity at those resonances. Our numerical results show that  $|R_{1s,2p}| \sim 10|R_{0,1s}| \sim 200|R_{0,2p}|$ . The small value of  $R_{0,2p}$  in the triple product of matrix elements is counteracted by a strong inter-exciton coupling and allows the  $p$  exciton to be visible in the shift conductivity spectrum with a similar brightness than the  $1s$  exciton. These selection rules have been treated previously in the second-harmonic generation optical response using analytical techniques<sup>77</sup>, and also by very recent ab initio calculations<sup>57</sup>. Above the quasi-particle gap, we observe the C resonance, whose shape is similar to the non-interacting case. Previous results based on tight-binding excitons<sup>10</sup> have shown that adding more bands to the calculation can enlarge the optical response of this part of the spectrum up to 25%. Calculations with larger Hilbert spaces, needed to converge this part of the spectrum, are postponed for future work.

As far as GeS is concerned, we focus our analysis on  $\sigma_{xxx}^{(sh)}$  and  $\sigma_{xyy}^{(sh)}$ , which are shown in Fig. 4a, b. The features of the IPA conductivities agree well with calculations in previous works<sup>36,53</sup>, regardless of the specific value of the band gap, which sets the optical onset for optical spectra. The  $\sigma_{xxx}^{(sh)}$  component shows that its main in-gap contribution comes from  $1s$ -like excitons, with opposite directionality. This fact can be understood by considering the non-interacting limit for the shift conductivity: the  $\Gamma$  and  $V_x$

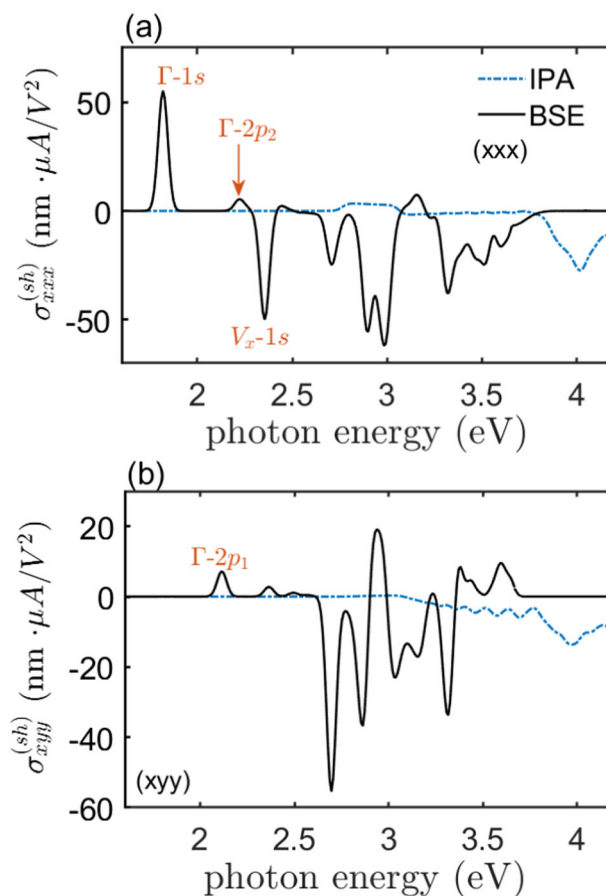


**Fig. 4 | Shift conductivity of monolayer GeS.** **a** Component  $xxx$  of the frequency-dependent shift conductivity tensor of monolayer GeS calculated in the IPA approximation and including exciton effects. **b** Same for the  $xyy$  component.

regions in the BZ give a contribution of different sign to the shift conductivity, which can be seen in the IPA curve around 3 eV. Thus, exciton formed in such regions inherit this feature. By inspecting excitonic matrix elements, we conclude that the  $\Gamma$ - $1s$  exciton has main contributions from the intra-exciton  $S_{\Gamma-1s,\Gamma-1s}$  and inter-exciton  $S_{\Gamma-2p_2,\Gamma-1s}$ . The former matrix element is two orders of magnitude larger than the equivalent one in MoS<sub>2</sub>. We attribute this difference to a larger effective mass occurring in monolayer GeS at  $\Gamma$  plus the large anisotropy effect, which make excitons in GeS depart from the hydrogen-like picture in the electron-hole interaction. As in MoS<sub>2</sub>, the  $\Gamma$ - $2p_2$  becomes bright in the shift conductivity spectrum. Our numerical results show that half of its response comes from the coupling  $S_{\Gamma-1s,\Gamma-2p_2}$  while the other half comes from the coupling with excitons at higher energies. Finally, we check that the  $V_x$ - $1s$  exciton response arise mainly from its intra-exciton coupling matrix elements. As shown in Supplementary Note 3, its wavefunction does not overlap with excitons formed around  $\Gamma$ , therefore the coupling with excitons at lower energies is vanishing. On the other hand,  $\sigma_{xyy}^{(sh)}$  shows little low-energy response, as no bright excitons can be coupled through the nonlinear oscillator strength. At higher energies, this tensor components reaches similar minimum values as the  $xxx$  component.

### Shift current in short-circuit

Finally, we consider incident light linearly polarized along the  $x$  direction, and evaluate the total photogalvanic (shift) current generated in a portion of a monolayer material of thickness  $d$  and width  $w$ . We focus on the longitudinal response, which reads<sup>26,78</sup>

$$J_x^{(2,DC)}(\omega) = \eta_{inc}(\omega) \cdot \eta_{abs}(\omega) \cdot G_{xxx}(\omega) \cdot w \cdot I_x(\omega), \quad (1)$$



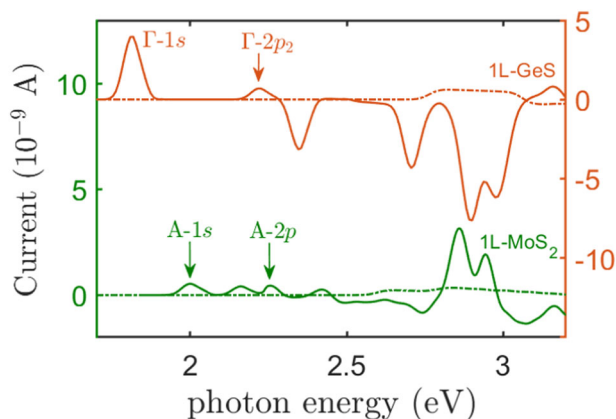


**Fig. 5 | Short-circuit current of monolayer MoS<sub>2</sub> and monolayer GeS.** Total shift current as occurring in a short-circuit configuration with 1L-MoS<sub>2</sub> and 1L-GeS<sub>2</sub>, under radiation with monochromatic light. We show the calculation with (solid line) and without (dashed) exciton effects.

where  $\eta_{\text{inc}}(\omega) = 1 - R(\omega)$ ,  $\eta_{\text{abs}}(\omega) = (1 - e^{-\alpha(\omega)d})$  and  $G_{\text{xxx}}(\omega) = 2\sigma_{\text{xxx}}^{(\text{sh})}(\omega)[\epsilon_0\alpha(\omega)]^{-1}$ , known as the *Glass coefficient*.  $R$  and  $\alpha$  stand for reflection and attenuation (or absorption) coefficients, respectively (see Supplementary note 1). Note that for both MoS<sub>2</sub> and GeS, the total current coincides with the longitudinal component in Eq. (1) ( $x$  being the armchair and  $c_2$  symmetry axis direction, respectively). In hexagonal 2D materials,  $R$  and  $\alpha$  are isotropic in-plane quantities, while for GeS they are computed by means of the dielectric tensor corresponding to the  $x$  direction. It has been argued<sup>78</sup> that the total current is minored if exciton effects are taken into account in calculations, as the magnitude of  $R$  and  $\alpha$  increases, which translates in less current in Eq. (1). However, the change in  $\sigma_{\text{abc}}^{(\text{sh})}$  after including exciton effects was not accounted for, which is crucial based on our previous analysis. In monolayer materials,  $\alpha(\omega)^{-1}$  is typically several orders of magnitude smaller than  $d$ . Therefore  $(1 - e^{-\alpha(\omega)d}) \simeq \alpha(\omega) \cdot d$  and, in the limit of a 2D sample (We numerically check that Eqs. (1) and (2) give nearly identical curves (not shown).), leads to

$$j_x^{(2,\text{DC})}(\omega) = \frac{\eta_{\text{inc}}(\omega)}{\epsilon_0} \cdot 2\sigma_{\text{xxx}}(\omega) \cdot I_x(\omega) \cdot d \cdot w, \quad (2)$$

which means that the exciton influence is ruled by the changes of the shift conductivity and the reflectivity factor. We assume an intensity of  $1.6 \times 10^4$  W/cm<sup>2</sup> and a sample width of  $2 \mu\text{m}$ , as in experiment<sup>25,26</sup>. We take a monolayer effective thickness for MoS<sub>2</sub> as reported in ref. 79, while we use the same value for GeS. Supplementary Fig. 1, we also compare our results for the reflectivity ratio with those obtained after reading the refractive index of ref. 79, showing a good agreement between the theoretical and experimental excitonic signatures.

In Fig. 5 we show the total current generated in a short-circuit configuration with samples of MoS<sub>2</sub> and GeS. We observe that in-gap 1s excitons give a response of  $\sim 0.5 \times 10^{-9}$  nA and  $\sim 5 \times 10^{-9}$  nA in MoS<sub>2</sub> and GeS, respectively, which corresponds to an enlargement by a factor of  $\sim 2$  and  $\sim 9$  with respect to the band-edge response predicted by the IPA calculation of each case. In general, the enhancement due to  $e$ - $h$  interactions in the total current is not as large as in the shift conductivity [see Figs. 1 and 4], due to an additional enhancement of the reflectivity ratio, i.e.,  $\eta_{\text{inc}}(\omega)$  is reduced in Eq. (1) and compensates changes in  $\sigma_{\text{xxx}}^{(\text{sh})}$ . Remarkably, the  $2p$  resonances in monolayer MoS<sub>2</sub> have a similar magnitude than the 1s. This is a consequence of the low oscillator strength of  $2p$  excitons, which gives low reflection at such energies. This feature is not as visible in the  $\Gamma$ - $2p_2$  resonance of GeS, since an optically bright exciton is close in energy and gives a considerable reflectivity. At energies in the continuum, near 3 eV, the response is enlarged to  $\sim 3$  nA in MoS<sub>2</sub>, while it is inverted in GeS reaching  $\sim -7$  nA (again be aware that more bands are needed to fully converge this part of the spectrum).

Photocurrent spectroscopy measurements in monolayer TMDCs allow for the measurement of excitonic resonances with linewidths as low as 8 meV<sup>80</sup>. Our results show that the  $p$  resonance in the shift photocurrent splits up by 100 meV from the B-1s exciton peak, and gives a comparable current response. It is thus of special importance to take into account the possible impact of this feature when interpreting photogalvanic measurements on TMDC-based experiments. While experimental measurements on WS<sub>2</sub> do not display any measurable shift-current response, a clear photogalvanic current (under circularly polarized light) is identified on ref. 30 in monolayer MoSe<sub>2</sub>, showing excitonic features. No doubt, more experiments are needed to characterize the exciton fine structure in the BPVE response in TMDC monolayer samples.

In summary, we have set up a methodology to calculate excitonic nonlinear optical responses based on Wannierized band structures combined with effective electron-hole model interactions. To perform the calculations, we have interfaced the output of the WANNIER90 code with our recently developed package XATU for solving the BSE. We have developed a post-processing code to calculate the optical response in the linear and second-order regimes. This methodology updates previous works on tight-binding excitons, now by using accurate wannierization of ab initio band structures. This provides several advantages: multiband effects are captured, the band structure is obtained accurately (including effective masses), and inter-site matrix elements are correctly accounted for. The examples covered in this work serve as a proof of concept to guide theoretical explorations in other materials. By extending the electron-hole interaction kernel beyond two dimensions, a large variety of systems can be addressed in future works.

The post-processing tools used in this work will be available soon in the next version of the XATU code<sup>61</sup>, via the package repository.

Note added. During the revision of this manuscript, another work has presented results for the low-energy shift conductivity of MoS<sub>2</sub> in presence of exciton effects<sup>52</sup>, showing good agreement with our results.

## Methods

### Ab initio band structure calculation

From a many-body perspective, the study of exciton physics in a gapped material requires first the evaluation of its quasi-particle band structure. To carry out this task, one typically introduces electron-electron interactions beyond the Kohn-Sham density functional theory (DFT) level by calculating a self-energy correction to the bands,  $\epsilon_n(\mathbf{k}) = \epsilon_n^{\text{KS}}(\mathbf{k}) + \Sigma_n(\mathbf{k})$ . The self-energy is typically obtained within the GW approximation<sup>8</sup>, where dynamical and local-field effects are included. Alternatively, hybrid-functionals can be used to obtain a satisfactory quasi-particle band structure (for instance, the band gaps are larger than those obtained from standard DFT) at lower computational cost than that of GW methods, as the dielectric matrix does not need to be explicitly calculated for the SRSH functional, and therefore making this method faster and requiring less memory<sup>81,82</sup>. Following this considerations, the first-principles band structures are calculated using a screened range-separated hybrid (SRSH) functional methodology as explained in refs. 66,67. The calculations of the SRSH functional parameters  $\alpha$  and  $\gamma$  were carried out with the Vienna Ab initio Simulation Package<sup>83,84</sup> (VASP). The GW type of the projector-augmented-wave pseudopotentials<sup>85,86</sup> (PAW), provided by VASP, have been used. PBE-based pseudopotentials were employed for Ge and S in GeS monolayer and bulk, using an energy cutoff of 650 eV. For MoS<sub>2</sub>, LDA-based pseudopotentials were used, see refs. 66,67, with an energy cutoff of 500 eV. The electronic configuration for the valence electrons of Mo is  $4s^2 4p^6 5s^1 4d^5$ ,  $3s^2 3p^4$  for S, and for Ge,  $3d^{10} 4s^2 4p^2$ .

The exact exchange  $\alpha$  and the range separated  $\gamma$  (in units of  $\text{\AA}^{-1}$ ) parameters of the SRSH were taken from ref. 67 for molybdenum disulfide (MoS<sub>2</sub>), being  $\alpha = 0.107$  and  $\gamma = 0.038 \text{ \AA}^{-1}$ . For GeS monolayer, the parameters of the SRSH were obtained following the procedure explained in

refs. 66,67. The  $G_0W_0$  calculations to get the reference band gap at the  $\Gamma$  point for GeS monolayer were done using a  $k$ -grid of  $15 \times 15 \times 1$  for the monolayer and  $10 \times 10 \times 4$  for the bulk, and 400 bands for both cases. The extrapolated band-gaps used as target for the SRSF functional for GeS are 2.62 eV and 1.63 eV for monolayer and bulk, respectively. The same  $k$ -grid was employed to get the parameters of the SRSF functional, obtaining  $\alpha = 0.107$  and  $\gamma = 0.030 \text{ \AA}^{-1}$  for the SRSF functional used in the case of GeS, as shown in Supplementary Fig 4. The tight-binding Hamiltonian needed for the input of the XATU code is obtained using the Wannier90<sup>69,70</sup> software interfaced with VASP. The DFT calculation is performed using VASP with the SRSF functional and the parameters  $\alpha$  and  $\gamma$  obtained as indicated previously.

The relaxation of the atomic coordinates at constant unit cell volume of the monolayers  $\text{MoS}_2$  and GeS were performed using the CRYSTAL<sup>87</sup> code. Final geometries are given in Supplementary Note 4.

### Wannier interpolation

After the self-consistent calculation, we consider a Wannier interpolation<sup>69,70</sup> to the starting quasi-particle band structure. First, a set of well-localized  $n_{\text{orb}}$  Wannier orbitals, which we denote  $w_{\alpha}(\mathbf{r} - \mathbf{d}_{\alpha} - \mathbf{R}) = \langle \mathbf{r} | \alpha \mathbf{R} \rangle$ , has to be found. Bloch states built with these functions,  $|\alpha \mathbf{k}\rangle = 1/\sqrt{N} \sum_{\mathbf{R}} e^{i\mathbf{k} \cdot \mathbf{R}} |\alpha \mathbf{R}\rangle$ , are referred to as Bloch-Wannier states. The single-particle Hamiltonian projected on these states is given by

$$H_{\alpha\alpha'}^{(W)}(\mathbf{k}) = \sum_{\mathbf{R}} e^{i\mathbf{k} \cdot \mathbf{R}} \langle \alpha \mathbf{0} | \hat{H} | \alpha' \mathbf{R} \rangle. \quad (3)$$

Note from the phase factor in (3) we choose the so-called *lattice* gauge, whereas the *atomic* gauge is another convention that is present in the literature<sup>88,89</sup> (See discussion around the WannierTools package: <https://www.wanniertools.org/theory/tight-binding-model/> (accessed May 2024)). Diagonalization of the  $n_{\text{orb}} \times n_{\text{orb}}$  Hamiltonian matrix yields the Wannier-interpolated energy eigenvalues,

$$[U^{\dagger}(\mathbf{k}) H^{(W)}(\mathbf{k}) U(\mathbf{k})]_{nn'} = \varepsilon_n(\mathbf{k}) \delta_{nn'}, \quad (4)$$

where  $U(\mathbf{k})$  is the unitary transformation matrix containing the Bloch eigenstates coefficients  $c_{n\alpha}(\mathbf{k})$  in the expansion of the band-structure eigenstates  $|n\mathbf{k}\rangle = \sum_{\alpha} c_{n\alpha}(\mathbf{k}) |\alpha \mathbf{k}\rangle$ .

We perform the wannier interpolation using the WANNIER90 package<sup>69,70</sup>. The trial orbitals for the initial projections in the  $\text{MoS}_2$  calculation were  $s$ ,  $p$ ,  $d$  and  $s$ ,  $p$  orbitals for Mo and S, respectively. For  $\text{MoS}_2$  we include SOC and we use a manifold of 34 bands, where we get 34 disentangled Wannier functions using the 26 highest valence bands, and the 8 lowest conduction bands. For the GeS monolayer, we use an initial manifold of 40 bands and construct 32 disentangled Wannier functions with 20 highest valence bands and 12 lowest conduction bands. The initial projections use the  $s$  and  $p$  orbitals for Ge and S.

Additionally, the Hamiltonian and dipole matrix elements between Wannier orbitals are printed, this is  $\langle \alpha \mathbf{0} | \hat{H} | \alpha' \mathbf{R} \rangle$  and  $\langle \alpha \mathbf{0} | \hat{r}_a | \alpha' \mathbf{R} \rangle$ , which is sufficient to evaluate all optical matrix elements at the IPA level.

### Bethe-Salpeter Equation

Excitons arise from the Coulomb interaction of a quasi-electron and quasi-hole, some of them forming bound states within the band-gap. Using valence ( $v$ ) and conduction ( $c$ ) single-particle states, we expand exciton states of zero center of mass momentum ( $\mathbf{Q} = 0$ ) in a basis of free electron-hole pairs as  $|X_N\rangle = \sum_{\mathbf{v}\mathbf{k}} A_{\mathbf{v}\mathbf{k}}^{(N)}(\mathbf{k}) \hat{c}_{\mathbf{v}\mathbf{k}}^{\dagger} \hat{c}_{\mathbf{v}\mathbf{k}} |0\rangle$ , being  $|0\rangle$  the ground state, identified as the Fermi sea. Exciton states are thus found by solving the BSE<sup>90</sup> in the Tamm-Dancoff approximation

$$(\varepsilon_{\mathbf{c}\mathbf{k}} - \varepsilon_{\mathbf{v}\mathbf{k}}) A_{\mathbf{v}\mathbf{k}}^{(N)}(\mathbf{k}) + \sum_{\mathbf{v}'\mathbf{k}'} \langle \mathbf{v}\mathbf{k} | K_{\text{eh}} | \mathbf{v}'\mathbf{k}' \rangle A_{\mathbf{v}'\mathbf{k}'}^{(N)}(\mathbf{k}) = E_N A_{\mathbf{v}\mathbf{k}}^{(N)}(\mathbf{k}), \quad (5)$$

where  $K_{\text{eh}} = -(D - X)$  is the electron-hole interaction kernel, including the direct ( $D$ ) and exchange terms ( $X$ ). The direct term reads

$$D_{\mathbf{v}\mathbf{k},\mathbf{v}'\mathbf{k}'}(\mathbf{k}, \mathbf{k}') = \int \psi_{\mathbf{c}\mathbf{k}}^*(\mathbf{r}) \psi_{\mathbf{v}'\mathbf{k}'}^*(\mathbf{r}') W(\mathbf{r}, \mathbf{r}') \psi_{\mathbf{c}\mathbf{k}'}(\mathbf{r}) \psi_{\mathbf{v}\mathbf{k}}(\mathbf{r}'), \quad (6)$$

and we treat the screened Coulomb interaction  $W$  in the static limit. The exchange term in the kernel is obtained by interchanging  $\mathbf{c}'\mathbf{k}'$  and  $\mathbf{v}\mathbf{k}$ . Fully ab initio calculations, namely GW-BSE methods, often employ an unscreened exchange interaction, as derived using many-body perturbation theory (MBPT) techniques<sup>90</sup>. Recent studies point out the necessity of constructing an effective screening for the exchange in some scenarios<sup>91</sup>, such as core-conduction excitations. In our variational approach where the BSE can be seen as the result of representing the Hamiltonian in a Hilbert space expanded by one-electron excitations Slater determinants, it is natural to assume the same screening for all Coulomb matrix elements<sup>11,92</sup>.

In this work, we model the 2D screening environment by using a Rytova-Keldysh potential<sup>93</sup>. In the case of vacuum surroundings, this model has one parameter, the screening length  $r_0$ , which can actually be calculated from DFT<sup>93</sup>. The choice of the 2D interaction model may be determinant for the resulting exciton energy series and the envelope wavefunctions (recent computational packages<sup>61,94</sup> allow to explore other different potentials). In the case of layered materials of much interest such as heterostructures or one-dimensional systems, other interaction models have also been proposed<sup>95,96</sup> and can be considered for future studies.

The Wannier orbitals  $w_{\alpha}(\mathbf{r} - \mathbf{d}_{\alpha} - \mathbf{R}) = \langle \mathbf{r} | \alpha \mathbf{R} \rangle$  have a finite spread that ideally may be smaller than the unit cell. To efficiently implement Eq. (6), here we ignore the real-space details of the orbitals, treating them as delta-like functions peaked at their centers<sup>10,59,61,94,97</sup>. The actual shape of the orbitals has been taken into consideration by other authors<sup>92</sup>, although we skip this numerical refinement in exchange for less computational and technical burden. The computational efficiency of this approach depends significantly on whether Coulomb integrals are performed in real or reciprocal space, as discussed in ref. 61. We use a real-space implementation<sup>59,61</sup>, which allows to cast the Coulomb interaction matrix elements in a bilinear form that is amenable for vectorizing calculations. In Sec. Results, we show that our results for the exciton structure in monolayer  $\text{MoS}_2$  are in agreement with previous literature, which is a successful test for our methodology.

### Exciton spectrum and wavefunctions

To include exciton effects through Eq. (5), the output of WANNIER90 is interfaced with our recently developed package XATU<sup>61</sup>, which yields the exciton energies and wavefunctions as output. The calculations are carried out using a dimension of  $N_k^2 \times n_v \times n_c = 102^2 \times 2 \times 2$  for the Hilbert space, where  $N_k$  is the number of  $k$  points in the Brillouin zone and  $n_v$  and  $n_c$  are the number of valence and conduction bands, respectively. For  $\text{MoS}_2$  we consider a screening length of  $r_0 = 35 \text{ \AA}$  and vacuum surroundings in the Rytova-Keldysh potential, similarly to previous studies<sup>98</sup>. In the case of GeS, we set the screening length to  $r_0 = 20 \text{ \AA}$ <sup>72</sup>. For a fair comparison between the non-interacting and excitonic results, we restrict to the same subspace of bands when evaluating the optical responses in both cases.

### Nonlinear optical response: shift current

In a general manner, the frequency-dependent second-order current-density reads

$$j_a^{(2)}(\omega) = \int d\omega_p \int d\omega_q \sum_{bc} \sigma_{abc}^{(2)}(\omega; \omega_p, \omega_q) \times \varepsilon_b(\omega_p) \varepsilon_c(\omega_q) \delta[(\omega_p + \omega_q) - \omega] \quad (7)$$

The contribution to the BPVE can be extracted by taking the DC limit. Here, we focus on the response under radiation with linearly polarized light, known as shift current (in the absence of magnetic effects). The amount and directionality of the DC shift-current response depends on the frequency of

the incident pulse, which can be expressed in terms of the second-order conductivity tensor at zero frequency<sup>34,76,99</sup>:

$$j_a^{(2, \text{sh})} = 2 \sum_{bc} \text{Re} \left[ \sigma_{abc}^{(\text{sh})}(0, \omega, -\omega) \varepsilon_b(\omega) \varepsilon_c(-\omega) \right], \quad (8)$$

where we have considered radiation under monochromatic light. The shift conductivity tensor (or simply shift conductivity) can be derived either in the velocity or length light-matter interaction gauges. Only the latter choice ensures the fastest convergence rates as well as the most accurate spectra for any basis size, and is also free from low-frequency divergences (see ref. 73 and references therein). In the IPA, the shift conductivity tensor reads

$$\sigma_{abc}^{(\text{sh})}(0, \omega, -\omega) = -\frac{ie^3}{2\hbar V} \sum_{mn'k} f_{mn'k} [I_{mn'k}^{abc} + I_{mn'k}^{acb}] \times \delta(\omega - \omega_{mn'k}), \quad (9)$$

where the strength of the transitions is  $I_{mn'k}^{abc} = r_{mn'k}^b r_{n'nk}^{c;a}$ , and the matrix elements are

$$r_{mn'k}^a = (1 - \delta_{mn'}) \xi_{mn'k}^a, \quad r_{mn'k}^{a;b} = \nabla_b r_{mn'k}^a - i r_{mn'k}^a \left[ \xi_{mn'k}^b - \xi_{n'nk}^b \right], \quad (10)$$

being  $\xi_{mn'k}^a$  the Berry connection and  $r_{mn'k}^{a;b}$  the generalized derivative of  $r_{mn'k}^a$ . For bulk systems, the shift conductivity tensor in Eq. (9) is usually reported in units of  $\mu A/V^2$ , while in this work we use the sheet units  $\text{nm} \cdot \mu A/V^2$ , and therefore  $V$  becomes the area of the crystal in Eq. (9). One thus avoid using a somewhat arbitrary thickness in 2D systems, particularly in planar ones.

While the off-diagonal Berry connections can be related to matrix elements of velocity operator, the generalized derivative presents the issue of computing the diagonal elements  $\xi_{mn'k}^a$ , which suffer from phase indetermination in numerical approaches. To circumvent this problem, an alternative approach is the use of sum rules<sup>73</sup> to directly evaluate  $r_{mn'k}^{a;b}$ , a procedure which only relies in using velocity matrix elements between energetically remote energy bands. It is thus desirable to perform the Wannierization in a large energy window enclosing the band gap, including as many remote bands as possible<sup>63</sup>. However, in this work we evaluate generalized derivatives by straightforward numerical  $k$  differentiation of eigenvectors, which will also help us later to evaluate excitonic matrix elements. To do so, we first set a differentiable gauge, as detailed in the next subsection within Sec. Methods. At a given frequency, for instance close to the band-gap, only the bands (and eigenstates) involved in the direct optical transitions are responsible for the SC value at such frequency. As long as these bands and eigenstates are well interpolated in the wannierization procedure, the resulting value for the shift conductivity is expected to be reliable independently of the number of remote bands, as they do not come into play. This fact has been explicitly checked in another work also using a method that does not involve a sum rule<sup>100</sup>.

In a similar fashion, a version of Eq. (9) including exciton effects can be written (see refs. 101,102 and Supplementary Note 5) but now involving matrix elements between excitonic many-body states. We extract the shift conductivity by taking the real part of the second order conductivity tensor at zero frequency<sup>102</sup>

$$\sigma_{abc}^{(\text{sh})}(0, \omega, -\omega) = \frac{\pi e^3}{\hbar V} \sum_{NN'} \text{Re} \left[ S_{NN'}^{abc} \right] \times [\delta(\hbar\omega - E_N) + \delta(\hbar\omega + E_N)]. \quad (11)$$

where we have defined the exciton coupling matrix element  $S_{NN'}^{abc} \equiv R_{0N}^a R_{NN'}^b R_{N'0}^c$ , being  $R_{0N}^a = \langle 0 | \hat{r}_a | X_N \rangle$  and  $R_{NN'}^a = \langle X_N | \hat{r}_a | X_{N'} \rangle$  with denoting the ground state. Further details about excitonic matrix elements are given in Supplementary Note 6. The same phase criteria is applied to single-particle eigenvectors (see again below in Sec. Methods) when

constructing the BSE matrix in Eq. (5) (note that it depends on the single-particle eigenvectors via the direct and exchange terms), which allows to agree on the phase choice between  $A_{\text{vck}}^{(N)}$  and single-particle matrix elements, ensuring that exciton matrix elements are properly evaluated.

### Smooth gauge for wavefunctions

In this section we give details on the evaluation of matrix elements and the gauge fixing on non-interacting Bloch states. This is needed to evaluate both shift conductivities with and without exciton, Eqs. (9) and (11), without the aid of any sum rule. We start by evaluating the velocity matrix elements (VMEs) between Bloch eigenstates,  $v_{mn'k}^a = i\hbar^{-1} \langle n\mathbf{k} | [\hat{H}, \hat{r}_a] | n'\mathbf{k} \rangle$ , following our previous work<sup>76,89</sup>. To do so, we extract Hamiltonian and position matrix elements between Wannier orbitals using the WANNIER90 package<sup>69,70</sup>.

Next, Berry connections  $\xi_{mn'k}^a = i \langle u_{n\mathbf{k}} | \nabla_a u_{n'\mathbf{k}} \rangle$  can be related to VMEs in the non-diagonal case ( $n \neq n'$ ) as

$$\xi_{mn'k}^a = -i \omega_{mn'k} v_{mn'k}^a. \quad (12)$$

For the diagonal case, one may expand in the Wannier coefficients to obtain ( $n = n'$ )

$$\xi_{nnk}^a = [U^\dagger(\mathbf{k}) \nabla_a U(\mathbf{k})]_{nn} + [U^\dagger(\mathbf{k}) \xi^{a(W)}(\mathbf{k}) U(\mathbf{k})]_{nn}, \quad (13)$$

where  $\xi_{\alpha\alpha\mathbf{k}}^{a(W)} = i \langle u_{\alpha\mathbf{k}}^{(W)} | \nabla_a u_{\alpha\mathbf{k}}^{(W)} \rangle$  is the Berry connection in the Bloch-Wannier basis.

The first term in Eq. (13) gives trouble if  $U(\mathbf{k})$  is found by numerical diagonalization. The eigenvector coefficients  $U_{\alpha n}(\mathbf{k})$  can contain a  $k$ -local random phase, that is not continuous in general, and therefore hinders the calculation of the numerical derivative in reciprocal space. To set a smooth gauge that allows numerical derivatives, we follow the following procedure (see also ref. 76). Assuming that  $U_{\alpha n}(\mathbf{k})$  are obtained through a numerical diagonalization, we define a new set of eigenvectors coefficients such that  $\tilde{U}_{\alpha n}(\mathbf{k}) = e^{-i\theta_{n\mathbf{k}}} U_{\alpha n}(\mathbf{k})$ . The local-phase factor is found by requiring that the sum of coefficients of an eigenvector in the Wannier Bloch basis to be real positive (i.e., equal to its modulus). By considering

$$\sum_{\alpha} U_{\alpha n}(\mathbf{k}) = \left| \sum_{\alpha} U_{\alpha n}(\mathbf{k}) \right| e^{i\theta_{n\mathbf{k}}}, \quad (14)$$

the phase  $e^{-i\theta_{n\mathbf{k}}}$  can be extracted. This criteria has been used previously to set a phase agreement between single-particle and consecutive many-body calculations<sup>10,90,92</sup>. Here, we empirically note that such this criteria also sets a local smooth gauge that allows the numerical evaluation of Eq. (13). Still, differentiation of eigenstate coefficients  $\tilde{U}_{\alpha n}(\mathbf{k})$  may produce discontinuities at band crossing points or lines along the BZ, depending on the sampling of the  $k$  grid. A plausible option is removing the  $k$  grid points where degeneracies, accidental or essential appear<sup>76</sup>. In Supplementary Note 7, we study the effect of the threshold energy used to identify them. Another gauge-fixing procedure has also been followed in the study of nonlinear optical responses<sup>33</sup> in the length gauge, although the role of degeneracies has not been discussed.

### Code availability

The BSE was solved using the XATU code, available at <https://github.com/xatu-code>. The code to evaluate nonlinear optical responses will be released soon as a post-processing tool for XATU.

Received: 28 June 2024; Accepted: 19 December 2024;  
Published online: 13 January 2025

### References

- Chopra, N. G. et al. Boron nitride nanotubes. *Science* **269**, 966 (1995).
- Wang, F., Dukovic, G., Brus, L. E. & Heinz, T. F. The optical resonances in carbon nanotubes arise from excitons. *Science* **308**, 838 (2005).



3. Mak, K. F., Lee, C., Hone, J., Shan, J. & Heinz, T. F. Atomically thin MoS<sub>2</sub>: a new direct-gap semiconductor. *Phys. Rev. Lett.* **105**, 136805 (2010).
4. Li, Y. et al. Measurement of the optical dielectric function of monolayer transition-metal dichalcogenides: MoS<sub>2</sub>, MoSe<sub>2</sub>, WS<sub>2</sub>, and WSe<sub>2</sub>. *Phys. Rev. B* **90**, 205422 (2014).
5. Wirtz, L., Marini, A. & Rubio, A. Excitons in boron nitride nanotubes: dimensionality effects. *Phys. Rev. Lett.* **96**, 126104 (2006).
6. Ramasubramanian, A. Large excitonic effects in monolayers of molybdenum and tungsten dichalcogenides. *Phys. Rev. B* **86**, 115409 (2012).
7. Qiu, D. Y., da Jornada, F. H. & Louie, S. G. Optical spectrum of MoS<sub>2</sub>: many-body effects and diversity of exciton states. *Phys. Rev. Lett.* **111**, 216805 (2013).
8. Martin, R. M., Reining, L. & Ceperley, D. M. Interacting electrons (Cambridge University Press, 2016).
9. Trolle, M. L., Seifert, G. & Pedersen, T. G. Theory of excitonic second-harmonic generation in monolayer MoS<sub>2</sub>. *Phys. Rev. B* **89**, 235410 (2014).
10. Ridolfi, E., Lewenkopf, C. H. & Pereira, V. M. Excitonic structure of the optical conductivity in MoS<sub>2</sub> monolayers. *Phys. Rev. B* **97**, 205409 (2018).
11. Bieniek, M., Szulakowska, L. & Hawrylak, P. Band nesting and exciton spectrum in monolayer MoS<sub>2</sub>. *Phys. Rev. B* **101**, 125423 (2020).
12. Qiu, D. Y., da Jornada, F. H. & Louie, S. G. Screening and many-body effects in two-dimensional crystals: Monolayer MoS<sub>2</sub>. *Phys. Rev. B* **93**, 235435 (2016).
13. Marsili, M., Molina-Sánchez, A., Palummo, M., Sangalli, D. & Marini, A. Spinorial formulation of the GW-BSE equations and spin properties of excitons in two-dimensional transition metal dichalcogenides. *Phys. Rev. B* **103**, 155152 (2021).
14. Molina-Sánchez, A., Palummo, M., Marini, A. & Wirtz, L. Temperature-dependent excitonic effects in the optical properties of single-layer MoS<sub>2</sub>. *Phys. Rev. B* **93**, 155435 (2016).
15. Sturman, B. & Fridkin, V. Photovoltaic and photo-refractive effects in noncentrosymmetric materials (Gordon and Breach Science Publishers, 1992).
16. Dai, Z. & Rappe, A. M. Recent progress in the theory of bulk photovoltaic effect. *Chem. Phys. Rev.* **4**, 011303 (2023).
17. Koch, W., Munser, R., Ruppel, W. & Würfel, P. Bulk photovoltaic effect in BaTiO<sub>3</sub>. *Solid State Commun.* **17**, 847 (1975).
18. Koch, W., Munser, R., Ruppel, W. & Würfel, P. Anomalous photovoltage in BaTiO<sub>3</sub>. *Ferroelectrics* **13**, 305 (1976).
19. von Baltz, R. & Kraut, W. Theory of the bulk photovoltaic effect in pure crystals. *Phys. Rev. B* **23**, 5590 (1981).
20. Batirov, T., Doubrovik, E., Djalalov, R. & Fridkin, V. The bulk photovoltaic effect in the piezoelectric crystal Pr<sub>3</sub>Ga<sub>5</sub>SiO<sub>14</sub>. *Ferroelectr. Lett. Sect.* **23**, 95 (1997).
21. Fridkin, V. et al. The bulk photovoltaic effect in LiNbO<sub>3</sub>, crystals under x-ray synchrotron radiation. *Ferroelectr. Lett. Sect.* **16**, 1 (1993).
22. Hornung, D., von Baltz, R. & Rössler, U. Band structure investigation of the bulk photovoltaic effect in n-gap. *Solid State Commun.* **48**, 225 (1983).
23. Buse, K. Light-induced charge transport processes in photorefractive crystals II: materials. *Appl. Phys. B* **64**, 391 (1997).
24. Spanier, J. E. et al. Power conversion efficiency exceeding the Shockley–Queisser limit in a ferroelectric insulator. *Nat. Photonics* **10**, 611 (2016).
25. Zhang, Y. et al. Enhanced intrinsic photovoltaic effect in tungsten disulfide nanotubes. *Nature* **570**, 349 (2019).
26. Krishna, J., Garcia-Goicelaya, P., de Juan, F. & Ibañez-Azpiroz, J. Understanding the large shift photocurrent of WS<sub>2</sub> nanotubes: a comparative analysis with monolayers. *Phys. Rev. B* **108**, 165418 (2023).
27. Xue, G. et al. WS<sub>2</sub> ribbon arrays with defined chirality and coherent polarity. *Science* **384**, 1100 (2024).
28. Dong, Y. et al. Giant bulk piezophotovoltaic effect in 3R-MoS<sub>2</sub>. *Nat. Nanotechnol.* **18**, 36 (2023).
29. Sun, R.-X. et al. Strain-prompted giant flexo-photovoltaic effect in two-dimensional violet phosphorene nanosheets. *ACS Nano* **18**, 13298 (2024).
30. Quereda, J. et al. Symmetry regimes for circular photocurrents in monolayer MoSe<sub>2</sub>. *Nat. Commun.* **9**, 3346 (2018).
31. Chang, Y.-R. et al. Shift current photovoltaics based on a noncentrosymmetric phase in in-plane ferroelectric SnS. *Adv. Mater.* **35**, 2301172 (2023).
32. Liang, Z. et al. Strong bulk photovoltaic effect in engineered edge-embedded van der Waals structures. *Nat. Commun.* **14**, 4230 (2023).
33. Zhou, Y. et al. Giant intrinsic photovoltaic effect in one-dimensional van der Waals grain boundaries. *Nat. Commun.* **15**, 501 (2024).
34. Sipe, J. E. & Shkrebtii, A. I. Second-order optical response in semiconductors. *Phys. Rev. B* **61**, 5337 (2000).
35. Young, S. M. & Rappe, A. M. First principles calculation of the shift current photovoltaic effect in ferroelectrics. *Phys. Rev. Lett.* **109**, 116601 (2012).
36. Rangel, T. et al. Large bulk photovoltaic effect and spontaneous polarization of single-layer monochalcogenides. *Phys. Rev. Lett.* **119**, 067402 (2017).
37. Cook, A. M., M. Fregoso, B., De Juan, F., Coh, S. & Moore, J. E. Design principles for shift current photovoltaics. *Nat. Commun.* **8**, 14176 (2017).
38. Tan, L. Z. et al. Shift current bulk photovoltaic effect in polar materials—hybrid and oxide perovskites and beyond. *Npj Comput. Mater.* **2**, 1 (2016).
39. Xiao, R.-C. et al. Non-synchronous bulk photovoltaic effect in two-dimensional interlayer-sliding ferroelectrics. *npj Comput. Mater.* **8**, 138 (2022).
40. Sauer, M. O. et al. Shift current photovoltaic efficiency of 2D materials. *npj Comput. Mater.* **9**, 35 (2023).
41. Zhang, Y. et al. Switchable magnetic bulk photovoltaic effect in the two-dimensional magnet CrI<sub>3</sub>. *Nat. Commun.* **10**, 3783 (2019).
42. Zhang, C., Guo, P. & Zhou, J. Tailoring bulk photovoltaic effects in magnetic sliding ferroelectric materials. *Nano Lett.* **22**, 9297 (2022).
43. Chaudhary, S., Lewandowski, C. & Refael, G. Shift-current response as a probe of quantum geometry and electron–electron interactions in twisted bilayer graphene. *Phys. Rev. Res.* **4**, 013164 (2022).
44. Kaplan, D., Holder, T. & Yan, B. Twisted photovoltaics at terahertz frequencies from momentum shift current. *Phys. Rev. Res.* **4**, 013209 (2022).
45. Sotome, M. et al. Spectral dynamics of shift current in ferroelectric semiconductor SbSI. *Proc. Natl Acad. Sci.* **116**, 1929 (2019).
46. Ni, Z. et al. Giant topological longitudinal circular photo-galvanic effect in the chiral multifold semimetal CoSi. *Nat. Commun.* **12**, 154 (2021).
47. Puente-Uribe, A. R., Tsirkin, S. S., Souza, I. & Ibañez-Azpiroz, J. Ab initio study of the nonlinear optical properties and dc photocurrent of the Weyl semimetal TaIrTe<sub>4</sub>. *Phys. Rev. B* **107**, 205204 (2023).
48. Sotome, M. et al. Terahertz emission spectroscopy of ultrafast exciton shift current in the noncentrosymmetric semiconductor CdS. *Phys. Rev. B* **103**, L241111 (2021).
49. Sturman, B. I. Ballistic and shift currents in the bulk photovoltaic effect theory. *Phys.-Uspekhi* **63**, 407 (2020).
50. Huang, Y.-S., Chan, Y.-H. & Guo, G.-Y. Large shift currents via in-gap and charge-neutral excitons in a monolayer and nanotubes of BN. *Phys. Rev. B* **108**, 075413 (2023).
51. Konabe, S. Exciton effect on shift current in single-walled boron-nitride nanotubes. *Phys. Rev. B* **103**, 075402 (2021).



52. Lai, M., Xuan, F. & Quek, S. Y. The bulk photovoltaic effect: Origin of shift currents in the many-body picture <https://arxiv.org/abs/2402.02002> (2024).
53. Chan, Y.-H., Qiu, D. Y., da Jornada, F. H. & Louie, S. G. Giant exciton-enhanced shift currents and direct current conduction with subbandgap photo excitations produced by many-electron interactions. *Proc. Natl Acad. Sci.* **118**, e1906938118 (2021).
54. Hu, C., Naik, M. H., Chan, Y.-H., Ruan, J. & Louie, S. G. Light-induced shift current vortex crystals in moiré heterobilayers. *Proc. Natl Acad. Sci.* **120**, e2314775120 (2023).
55. Grüning, M. & Attacalite, C. Second harmonic generation in *h*-bn and *moS*<sub>2</sub> monolayers: Role of electron-hole interaction. *Phys. Rev. B* **89**, 081102 (2014).
56. Attacalite, C., Nguer, A., Cannuccia, E. & Grüning, M. Strong second harmonic generation in sic, zno, gan two-dimensional hexagonal crystals from first-principles many-body calculations. *Phys. Chem. Chem. Phys.* **17**, 9533 (2015).
57. Ruan, J., Chan, Y. H. & Louie, S. G. Excitonic effects in nonlinear optical responses: exciton-state formalism and first-principles calculations. <https://arxiv.org/abs/2310.09674> (2023).
58. García-Goiricelaya, P., Krishna, J. & Ibañez Azpiroz, J. Including many-body effects into the wannier-interpolated quadratic photoresponse tensor. *Phys. Rev. B* **107**, 205101 (2023).
59. Wu, F., Qu, F. & MacDonald, A. H. Exciton band structure of monolayer *MoS*<sub>2</sub>. *Phys. Rev. B* **91**, 075310 (2015).
60. Galvani, T. et al. Excitons in boron nitride single layer. *Phys. Rev. B* **94**, 125303 (2016).
61. Uría-Álvarez, A. J., Esteve-Paredes, J. J., García-Blázquez, M. & Palacios, J. J. Efficient computation of optical excitations in two-dimensional materials with the xatu code. *Comput. Phys. Commun.* **295**, 109001 (2024).
62. Wang, C. et al. First-principles calculation of nonlinear optical responses by Wannier interpolation. *Phys. Rev. B* **96**, 115147 (2017).
63. Ibañez-Azpiroz, J., Tsirkin, S. S. & Souza, I. Ab initio calculation of the shift photocurrent by Wannier interpolation. *Phys. Rev. B* **97**, 245143 (2018).
64. Ibañez-Azpiroz, J., de Juan, F. & Souza, I. Assessing the role of interatomic position matrix elements in tight-binding calculations of optical properties. *SciPost Phys.* **12**, 070 (2022).
65. Nguyen, L. T. & Makov, G. Ges phases from first-principles: structure prediction, optical properties, and phase transitions upon compression. *Cryst. Growth Des.* **22**, 4956–4969 (2022).
66. Ramasubramaniam, A., Wing, D. & Kronik, L. Transferable screened range-separated hybrids for layered materials: the cases of *MoS*<sub>2</sub> and *h*-BN. *Phys. Rev. Mater.* **3**, 084007 (2019).
67. Camarasa-Gómez, M., Ramasubramaniam, A., Neaton, J. B. & Kronik, L. Transferable screened range-separated hybrid functionals for electronic and optical properties of van der Waals materials. *Phys. Rev. Mater.* **7**, 104001 (2023).
68. Dien, V. K. et al. Unlocking the potential of ges monolayer: Strain-enabled control of electronic transports and exciton radiative lifetimes. <https://arxiv.org/abs/2306.04914> (2023).
69. Mostofi, A. A. et al. wannier90: a tool for obtaining maximally-localised Wannier functions. *Comput. Phys. Commun.* **178**, 685 (2008).
70. Pizzi, G. et al. Wannier90 as a community code: new features and applications. *J. Phys. Condens. Matter* **32**, 165902 (2020).
71. Qiu, D. Y., Cao, T. & Louie, S. G. Nonanalyticity, valley quantum phases, and lightlike exciton dispersion in monolayer transition metal dichalcogenides: theory and first-principles calculations. *Phys. Rev. Lett.* **115**, 176801 (2015).
72. Gomes, L. C., Trevisanutto, P. E., Carvalho, A., Rodin, A. S. & Castro Neto, A. H. Strongly bound mott-wannier excitons in *GeS* and *GeSe* monolayers. *Phys. Rev. B* **94**, 155428 (2016).
73. Taghizadeh, A., Hipolito, F. & Pedersen, T. G. Linear and nonlinear optical response of crystals using length and velocity gauges: effect of basis truncation. *Phys. Rev. B* **96**, 195413 (2017).
74. Zhang, F. et al. Intervalley excitonic hybridization, optical selection rules, and imperfect circular dichroism in monolayer *h*-BN. *Phys. Rev. Lett.* **128**, 047402 (2022).
75. Quintela, M. F. C. M. & Pedersen, T. G. Anisotropic linear and nonlinear excitonic optical properties of buckled monolayer semiconductors. *Phys. Rev. B* **107**, 235416 (2023).
76. García-Blázquez, M. A., Esteve-Paredes, J. J., Uría-Álvarez, A. J. & Palacios, J. J. Shift current with gaussian basis sets and general prescription for maximally symmetric summations in the irreducible Brillouin zone. *J. Chem. Theory Comput.* **19**, 9416 (2023).
77. Taghizadeh, A. & Pedersen, T. G. Nonlinear optical selection rules of excitons in monolayer transition metal dichalcogenides. *Phys. Rev. B* **99**, 235433 (2019).
78. Fei, R., Tan, L. Z. & Rappe, A. M. Shift-current bulk photovoltaic effect influenced by quasiparticle and exciton. *Phys. Rev. B* **101**, 045104 (2020).
79. Liu, H.-L. et al. Temperature-dependent optical constants of monolayer *MoS*<sub>2</sub>, *MoSe*<sub>2</sub>, *WS*<sub>2</sub>, and *WSe*<sub>2</sub>: spectroscopic ellipsometry and first-principles calculations. *Sci. Rep.* **10**, 15282 (2020).
80. Vaquero, D. et al. Excitons, trions and rydberg states in monolayer *MoS*<sub>2</sub> revealed by low-temperature photocurrent spectroscopy. *Commun. Phys.* **3**, 194 (2020).
81. Gerosa, M. et al. Electronic structure and phase stability of oxide semiconductors: performance of dielectric-dependent hybrid functional dft, benchmarked against gw band structure calculations and experiments. *Phys. Rev. B* **91**, 155201 (2015).
82. Tal, A., Liu, P., Kresse, G. & Pasquarello, A. Accurate optical spectra through time-dependent density functional theory based on screening-dependent hybrid functionals. *Phys. Rev. Res.* **2**, 032019 (2020).
83. Kresse, G. & Furthmüller, J. Efficiency of ab-initio total energy calculations for metals and semiconductors using a plane-wave basis set. *Comput. Mater. Sci.* **6**, 15 (1996).
84. Kresse, G. & Furthmüller, J. Efficient iterative schemes for ab initio total-energy calculations using a plane-wave basis set. *Phys. Rev. B* **54**, 11169 (1996).
85. Blöchl, P. E. Projector augmented-wave method. *Phys. Rev. B* **50**, 17953 (1994).
86. Kresse, G. & Joubert, D. From ultrasoft pseudopotentials to the projector augmented-wave method. *Phys. Rev. B* **59**, 1758 (1999).
87. Erba, A. et al. Crystal23: a program for computational solid state physics and chemistry. *J. Chem. Theory Comput.* **19**, 6891 (2022).
88. Vanderbilt, D. Berry phases in electronic structure theory: electric polarization, orbital magnetization and topological insulators (Cambridge University Press, 2018).
89. Esteve-Paredes, J. J. & Palacios, J. J. A comprehensive study of the velocity, momentum and position matrix elements for Bloch states: application to a local orbital basis. *SciPost Phys. Core* **6**, 002.1 (2023).
90. Rohlfing, M. & Louie, S. G. Electron-hole excitations and optical spectra from first principles. *Phys. Rev. B* **62**, 4927 (2000).
91. Qiu, D., Chang Lee, V., Filip, M., Jornada, F. & McArthur, J. Hilbert-space separation schemes in energy-space and real-space for excited-state calculations. In: *APS March Meeting Abstracts*, vol. 2023, A59 (2023).
92. Bieniek, M., Sadecka, K., Szulakowska, L. & Hawrylak, P. Theory of excitons in atomically thin semiconductors: tight-binding approach. *Nanomaterials* **12**, 1582 (2022).
93. Cudazzo, P., Tokatly, I. V. & Rubio, A. Dielectric screening in two-dimensional insulators: implications for excitonic and impurity states in graphane. *Phys. Rev. B* **84**, 085406 (2011).

94. Dias, A. C., Silveira, J. F. & Qu, F. WanTiBEXOS: a Wannier based tight binding code for electronic band structure, excitonic and optoelectronic properties of solids. *Comput Phys. Commun.* **285**, 108636 (2023).
95. Kamban, H. C. & Pedersen, T. G. Interlayer excitons in van der Waals heterostructures: Binding energy, Stark shift, and field-induced dissociation. *Sci. Rep.* **10**, 5537 (2020).
96. Villegas, C. E. P. & Rocha, A. R. Screened hydrogen model of excitons in semiconducting nanoribbons. *Phys. Rev. B* **109**, 165425 (2024).
97. Maity, I., Mostofi, A. A. & Lischner, J. Atomistic theory of twist-angle dependent intralayer and interlayer exciton properties in twisted bilayer materials <https://arxiv.org/abs/2406.11098> (2024).
98. Berkelbach, T. C., Hybertsen, M. S. & Reichman, D. R. Theory of neutral and charged excitons in monolayer transition metal dichalcogenides. *Phys. Rev. B* **88**, 045318 (2013).
99. Ahn, J., Guo, G.-Y. & Nagaosa, N. Low-frequency divergence and quantum geometry of the bulk photovoltaic effect in topological semimetals. *Phys. Rev. X* **10**, 041041 (2020).
100. Wang, H., Tang, X., Xu, H., Li, J. & Qian, X. Generalized Wilson loop method for nonlinear light-matter interaction. *npj Quantum Mater.* **7**, 61 (2022).
101. Pedersen, T. G. Intraband effects in excitonic second-harmonic generation. *Phys. Rev. B* **92**, 235432 (2015).
102. Taghizadeh, A. & Pedersen, T. G. Gauge invariance of excitonic linear and nonlinear optical response. *Phys. Rev. B* **97**, 205432 (2018).

## Acknowledgements

The authors acknowledge financial support from the Spanish MICINN (grants nos. PID2019-109539GB-C43, TED2021-131323B-I00, and PID2022-141712NB-C21), the María de Maeztu Program for Units of Excellence in R&D (grant no. CEX2018-000805-M), the Comunidad Autónoma de Madrid through the Recovery, Transformation and Resilience Plan from Spain, the NextGenerationEU plan from the European Union (MAD2D-CM-UAM7), and the Generalitat Valenciana through Programa Prometeo (2021/017). The authors thankfully acknowledge RES resources provided by Universidad de Málaga in Picasso to FI-2024-2-0016. M.A. García-Blázquez acknowledges financial support from Universidad Autónoma de Madrid through an FPI-UAM grant. M.C.-G. is grateful to the Azrieli Foundation for the award of an Azrieli International Postdoctoral Fellowship. Additional computational resources were provided by the Weizmann Institute of Science at Chemfarm. M.C.-G. thanks Tonatiuh Rangel for providing the initial geometries of bulk and monolayer GeS.

## Author contributions

J.J.E.-P designed research; J.J.P supervised research; J.J.E.-P, M.A.G.-B, A.J.U.-A., and M.C.-G performed research; J.J.E.-P, M.A.G.-B, A.J.U.-A., M.C.-G, and J.J.P analyzed the data; and J.J.E.-P, M.A.G.-B, M.C.-G, and J.J.P wrote the manuscript.

## Competing interests

The authors declare no competing interest.

## Additional information

**Supplementary information** The online version contains supplementary material available at <https://doi.org/10.1038/s41524-024-01504-2>.

**Correspondence** and requests for materials should be addressed to J. J. Esteve-Paredes.

**Reprints and permissions information** is available at <http://www.nature.com/reprints>

**Publisher's note** Springer Nature remains neutral with regard to jurisdictional claims in published maps and institutional affiliations.

**Open Access** This article is licensed under a Creative Commons Attribution-NonCommercial-NoDerivatives 4.0 International License, which permits any non-commercial use, sharing, distribution and reproduction in any medium or format, as long as you give appropriate credit to the original author(s) and the source, provide a link to the Creative Commons licence, and indicate if you modified the licensed material. You do not have permission under this licence to share adapted material derived from this article or parts of it. The images or other third party material in this article are included in the article's Creative Commons licence, unless indicated otherwise in a credit line to the material. If material is not included in the article's Creative Commons licence and your intended use is not permitted by statutory regulation or exceeds the permitted use, you will need to obtain permission directly from the copyright holder. To view a copy of this licence, visit <http://creativecommons.org/licenses/by-nc-nd/4.0/>.

© The Author(s) 2025